Article

Dual S-Scheme Heterojunction CdS/TiO$_2$/g-C$_3$N$_4$ Photocatalyst for Hydrogen Production and Dye Degradation Applications

Muhammad Shoaib, Muhammad Yasin Naz, Shazia Shukrullah,* Muhammad Adnan Munir, Muhammad Irfan, Saifur Rahman, and Abdulnoor Ali Jazem Ghanim

Cite This: ACS Omega 2023, 8, 43139−43150

Read Online

ACCESS | Metrics & More | Article Recommendations

ABSTRACT: This study investigated a ternary CdS/TiO$_2$/g-C$_3$N$_4$ heterojunction for degrading synthetic dyes and hydrogen production from aqueous media through visible light-initiated photocatalytic reactions. CdS, TiO$_2$, and g-C$_3$N$_4$ were combined in different mass ratios through a simple hydrothermal method to create CdS/TiO$_2$/g-C$_3$N$_4$ composite photocatalysts. The prepared heterojunction catalysts were investigated by using FTIR, XRD, EDX, SEM, and UV−visible spectroscopy analysis for their crystal structures, functional groups, elemental composition, microtopography, and optical properties. The rhodamine B dye was then degraded by using fully characterized photocatalysts. The maximum dye degradation efficiency of 99.4% was noted in these experiments. The evolution rate of hydrogen from the aqueous solution with the CdS/TiO$_2$/g-C$_3$N$_4$ photocatalyst remained 2910 μmol·h^{-1}·g^{-1}, which is considerably higher than those of g-C$_3$N$_4$, CdS, CdS/g-C$_3$N$_4$, and g-C$_3$N$_4$/TiO$_2$-catalyzed reactions. This study also proposes a photocatalytic activity mechanism for the tested ternary CdS/TiO$_2$/g-C$_3$N$_4$ heterojunctions.
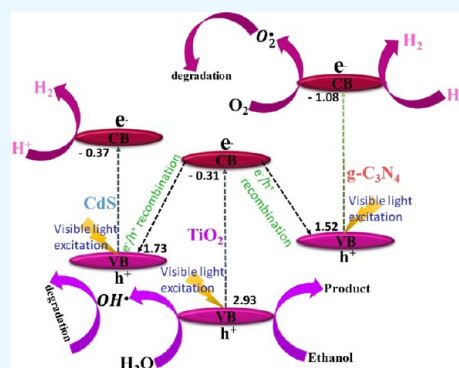
1. INTRODUCTION

Developing renewable energy sources using solar water splitting is crucial for producing an environmentally friendly hydrogen fuel. Researchers have worked hard to deduce photocatalytic methods for producing hydrogen from water ever since the earliest attempt at water splitting by photocatalysis on Pt/TiO$_2$ was performed in 1972. Many semiconductors, including TiO$_2$,[1] Cu$_2$O,[2] SrTiO$_3$,[3] ZnFe$_2$O$_4$,[4] CdS,[5] and InVO$_4$,[6] have been reported as photocatalysts for hydrogen production. Since photocatalysis effectively addresses the growing environmental concerns and energy crises, semiconductor photocatalysts have drawn much attention in the last few decades.[7] Many semiconductor photocatalysts were created to address environmental problems such as water contamination. Increasing environmental pollution, especially in aquatic atmospheres, requires new technologies and methods for eliminating and destroying various pollutants from subject material. In many cases, biological processes failed in achieving the desired results because some contaminants can withstand the natural and photocatalyzed degradation of contaminants under certain conditions. Contaminated wastewater treatment is essential for sustainable environment and quality of life.[8] Sun et al. discovered the light-driven redox process for solar water splitting and N$_2$ fixation.[9] The removal of environmental pollutants in the hydrate phase using photocatalysts has been hailed as an extremely efficient and eco-friendly method for wastewater remediation due to its

higher redox reactivity and use of solar irradiation as a reaction activation source.[10] However, because a high redox potential is required when the band gap is large, the particular constraints for each photocatalyst hamper the actual performance of individual semiconductors. At the same time, a small band gap is required for photocatalysts to respond to visible light.[11] Binary heterojunctions can also be constructed for water splitting and degradation to dyes. However, the electron−hole recombination in ternary heterojunctions is relatively slower than in binary heterojunctions, which boosts the separation of photoinduced charges much higher than in binary heterojunctions. The redox and oxidation potentials in ternary heterojunctions are also high, which is crucial for efficient photocatalysis processes. The carbon nitride in a ternary heterojunction carries excess electrons, which significantly expedites the hydrogen evolution process. Thus, carbon nitride-containing photocatalysts offer a more rapid reaction for hydrogen evolution.

Although the underlying charge transport mechanism of S-scheme photocatalysts is the same as that of direct Z-scheme
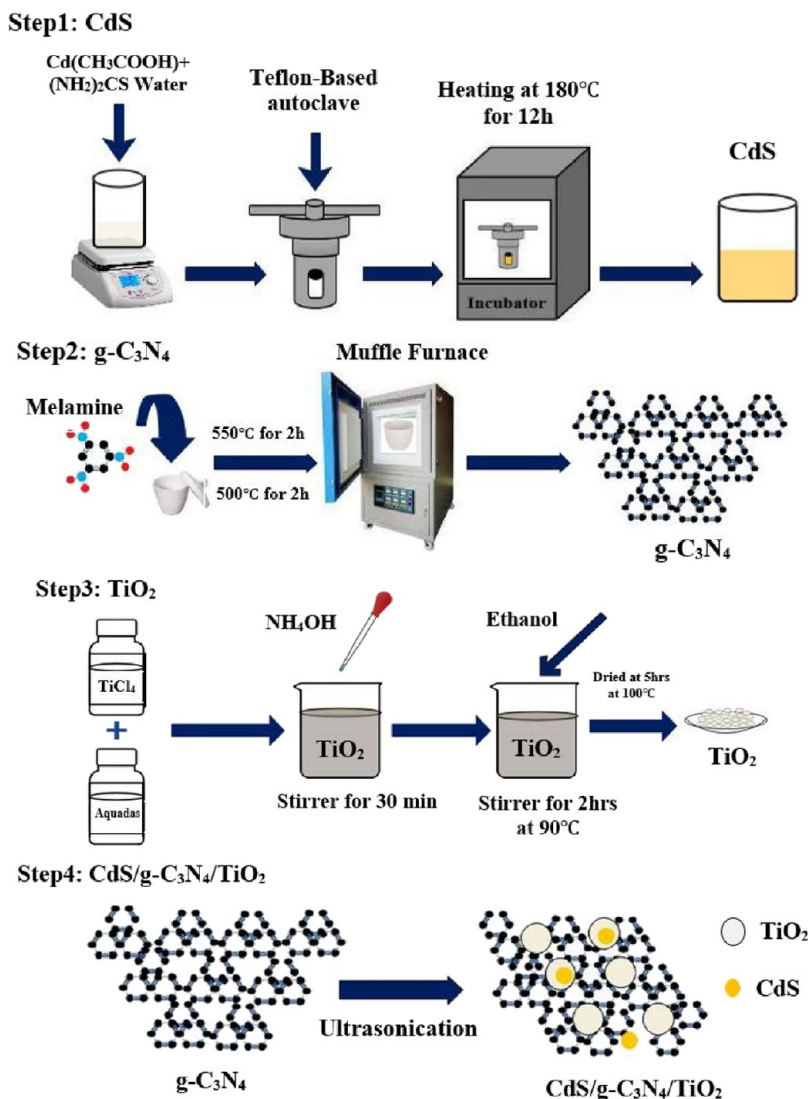
Scheme 1. Schematic of the Method of Synthesizing CdS/TiO$_2$/g-C$_3$N$_4$ Heterojunction

photocatalysts, they can transcend the drawbacks of all Z-scheme heterojunctions.[12] The S-scheme heterostructures can also override the drawbacks of unitary photocatalysts and type II heterosystems, expand the range of light absorption, and significantly advance the separation of charge carriers.[13] Recent research has focused on developing innovative S-scheme heterostructure photocatalysts with enhanced optoelectronic capabilities and a high density of redox sites for photocatalysis applications. Some of the reported studies on S-scheme heterosystems include Co$_9$S$_8$/In$_2$O$_3$,[14] g-C$_3$N$_4$/TiO$_2$,[15] MoO$_3$/g-C$_3$N$_4$,[16] and WO$_3$/g-C$_3$N$_4$,[17] which showed considerable tendency for photocatalytic H$_2$ evolution. Some recent studies have demonstrated that CdS is also an important component of ternary heterojunction due to a direct correlation between topological structure and various parameters of CdS.[18] CdS nanocrystals were produced using different techniques. The charge transfer mechanism, band configuration, and interfacial reactivity of CdS may change with the change in the synthesis technique. The majority of recent studies were conducted on photocatalytic reactions in water. The effectiveness of photocatalysis systems for separating salt water has not been widely reported. It is challenging to perform saltwater splitting on a large scale, as contaminants and ionic constituents in

saltwater significantly impact the activities and stability of the photocatalysts. The performance of the CdS material, which is highly active and stable, is critical in finding suitable candidates for solar saltwater splitting in the real world. Due to its favorable semiconductor features and appropriate band gap (2.69 eV), graphite carbon nitride material has been prepared and explored as a revolutionary nonmetallic semiconductor substance.[19] Water splitting for the production of H$_2$ and removal of organic contaminants can be performed more efficiently using g-C$_3$N$_4$ than other materials.[20] The most popular technique for producing g-C$_3$N$_4$ is thermal poly-condensation.[21] The primary precursors used to prepare g-C$_3$N$_4$ are dicyandiamide,[22] melamine,[23] urea,[24] and thiourea,[25] which are less costly than the materials used to produce other photocatalysts. Having a fast recombination rate of photo-induced charge species, pure g-C$_3$N$_4$ is ineffective as a photocatalyst. However, the catalytic efficacy of pristine g-C$_3$N$_4$ is low due to quick recombination of photoinduced charges, its small surface area, and other disadvantages. g-C$_3$N$_4$ is an n-type semiconductor with a conduction band (E_{CB}) at 1.08 V vs NHE and a valence band (E_{VB}) at 1.52 V vs NHE (E_g = 2.06 eV). TiO$_2$/g-C$_3$N$_4$ integration results in a unique composition with a high E_{VB} (2.93 V vs NHE) and a small E_{CB}

(0.31 V vs NHE), which can suppress the recombination of charges, increase light absorption, and boost redox potentials. The g-C_3N_4 has been combined with TiO_2 to build a photocatalyst that exhibited 3.5 times greater photocatalytic activity for H_2 production due to excellent migration and separation of charge carriers, wide optical response, and substantial reduction capacity.[16]

Although TiO_2 is one of the most effective photocatalytic semiconductors when exposed to UV light, it performs poorly when exposed to visible light.[26] The large band gap issue can be addressed by compositing TiO_2 with materials with a narrow band gap. CdS is a material with a comparatively small bandgap that may show good absorption in visible light spectrum. Because of this feature, CdS can harness sunlight in visible region for photocatalytic reactions. In the case of the CdS/TiO_2 photocatalyst, both CdS and TiO_2 are semiconductors that can harness light energy to catalyze various reactions. This research develops visible-light-driven single, binary and ternary photocatalysts for degrading RhB dye and producing hydrogen through water splitting. A set of CdS, g-C_3N_4, TiO_2 single catalysts, CdS/g-C_3N_4, g-C_3N_4/TiO_2 binary catalysts, and ternary catalyst (CdS/TiO_2/g-C_3N_4) was produced and tested for photocatalytic dye degradation and water splitting.

2. EXPERIMENTAL PROCEDURES

2.1. Fabrication of Ternary CdS/TiO_2/g-C_3N_4. In the first step, CdS was manufactured via a hydrothermal method. Typically, 2.5 mmol of cadmium acetate and 1.5 mmol of thiourea were mixed in 50 mL of DI water. Later, the prepared solution was continuously agitated for 50 min, and the acquired precursor was provided at 180 °C for 12 h in a 100 mL autoclave. The resulting yellow precipitate was then centrifuged four times and washed by utilizing ethanol and then by using DI water. After washing, the residue was dried for 10 h at 90 °C. The second step of Scheme 1 illustrates the catalyst synthesis method and associated steps. The method used to prepare g-C_3N_4 is described in the literature.[27] Melamine was treated at 550 °C for 2 h in a crucible. After the final product was cooled, it was crushed into yellow g-C_3N_4 powder. It was then exfoliated in 50 mL deionized water using an ultrasonic generator for 3 h to produce g-C_3N_4 nanosheets for other processes. Then, the $TiCl_4$ solution was combined with deionized water and stirred for 3 h using a magnetic stirrer. NH_4OH was added to the mixture while being stirred until it turned white. The residue was then dried for 30 min at 90 °C.

Step 3 of Scheme 1 shows the preparation of the TiO_2 nanoparticles. In the last step, the CdS/TiO_2/g-C_3N_4 ternary composite was fabricated by adopting the technique reported by Hashem et al.[28] First, the exact amounts of TiO_2 and g-C_3N_4 were distributed cooperatively in deionized water via ultrasonication for 1 h. After that, the powder was removed and repeatedly cleaned by using deionized water. g-C_3N_4/TiO_2 filter powder was obtained after drying at 100 °C. A typical process includes dissolving 0.003 g of CdS in 200 mL of DI water, adding 2.4 g of TiO_2/g-C_3N_4 to the mixture, and ultrasonically processing it for 60 min. The final CdS/TiO_2/C_3N_4 product was washed and heat treated 60 °C for 24 h. A similar procedure is followed to produce CdS/g-C_3N_4 and TiO_2/g-C_3N_4 photoactive catalysts.

2.2. Characterization of Catalysts. XRD analysis was utilized to deduce the structural characteristics of the fabricated specimens. A 2θ range of 20°−70° was used to obtain XRD spectra using Cu−K radiation (= 0.15418 nm). The functional groups on the photocatalyst surface were examined through FTIR spectroscopy by using a PerkinElmer Frontier spectrophotometer. Morphological and structural characterization of materials was achieved via SEM (Nova nano SEM 450). To obtain UV−vis spectra, a UV−vis spectrometer fitted with an integrating sphere was utilized, along with a typical model. Elemental analysis was conducted via X-ray energy-dispersive spectroscopy.

2.3. Photocatalytic Experiments. As nanocatalysts were developed, photocatalytic performance was calculated using visible irradiation exposure to eliminate Rhodamine B. The solutions were prepared by adding 50 mL of Rhodamine B (25 mg/L) in 10 mg of catalyst. The obtained solution was then continuously stirred for 1 h while being kept in the dark to achieve the equilibrium between adsorption and desorption. Using a 50 W LED lamp, samples were tested for their photocatalytic activity. The degradation rate was then examined by using UV−vis spectra, and any changes to the absorption spectra were noted. The RhB degradation was determined using Equation 1.

$$H = \frac{C_0 - C_t}{C_0} \times 100\%$$

$$(1)$$

where C_0 depicts the initial amount of RhB and C_t is the amount after an interval of time t. UV−vis investigation of RhB solution was executed to capture changes in the absorption spectra. A photocatalytic test system was employed to check hydrogen evolution from water splitting by using synthesized materials. The visible light source, used in this experiment, comprised a 300 Xe lamp. In a typical test, 100 mL of a solution containing a sacrificial agent (ethanol) was mixed with 10 mg of the photocatalyst and irradiated with a 300 Xe lamp. A gas analyzer was used to analyze the gaseous product from photocatalytic water splitting.

3. RESULTS AND DISCUSSION

3.1. Structural Investigation. A comparative examination of the X-ray diffraction spectra of CdS, g-C_3N_4, TiO_2, and hybrid CdS/g-C_3N_4, TiO_2/g-C_3N_4, and CdS/TiO_2/g-C_3N_4 composites is presented in Figure 1. XRD peaks of CdS matched well with JCPDS No. 10−0454. In this spectrum, (110), (111), and (112) crystallographic planes are assigned to peaks at 2θ values of 26.70°, 43.71°, and 52.20°.[29] At 2θ value of 27.4°, a sharp diffraction peak of (0 0 2) plane is linked to the interplanar stacking of aromatic compounds (JCPDS No. 87−1526).[30] The major anatase TiO_2 diffraction peaks well matched to (101), (004), (200), (105), and (204) crystal planes at 2θ values of 25.4°5, 37.99°, 48.06°, 53.03°, and 63.02° (JCPDS No. 21−1272). It was evident from the XRD pattern of the CdS/TiO_2/g-C_3N_4 nanocomposite that diffraction peaks of g-C_3N_4, CdS, and TiO_2 are presented in the spectrum. It confirms that CdS and TiO_2 have successfully embedded into the g-C_3N_4 and TiO_2 composite as the interlayer periodic stowing of g-C_3N_4 declines after mixing with CdS.[31] The diffraction peaks for CdS, g-C_3N_4 and TiO_2 confirmed the creation of heterostructure amalgamations in the nanocomposite.

3.2. Morphology and Elemental Composition of Photocatalysts. Figure 2 reveals the surface morphologies from the SEM micrographs of synthesized CdS, g-C_3N_4, TiO_2,
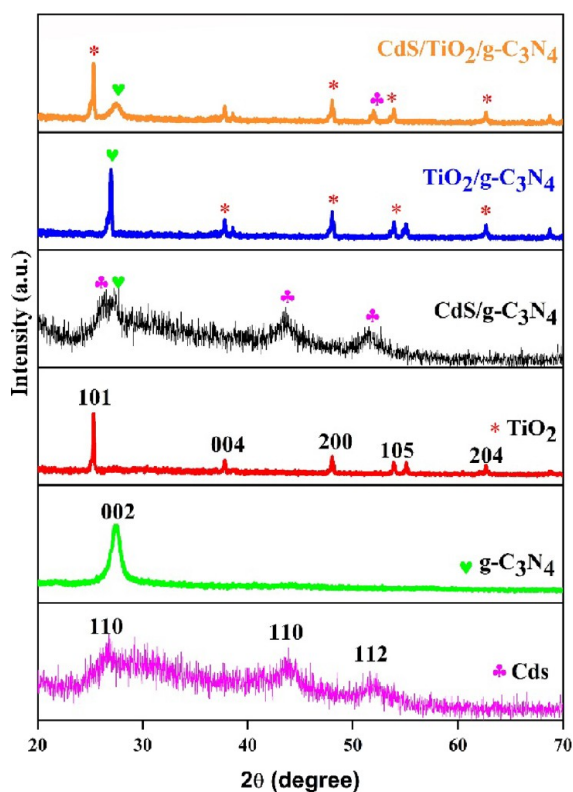
Figure 1. Diffraction spectra of CdS, g-C$_3$N$_4$, TiO$_2$, CdS/g-C$_3$N$_4$, TiO$_2$/g-C$_3$N$_4$, and CdS/TiO$_2$/g-C$_3$N$_4$.

and CdS/TiO$_2$/g-C$_3$N$_4$ composites. Figure 2a shows nanoparticles of pure CdS tightly aggregated into irregularly shaped particles. SEM micrographs of g-C$_3$N$_4$ demonstrate sheet-like layered structures. The significant aggregation and larger particles with some curled structures in g-C$_3$N$_4$ are visible in Figure 2b. The manufactured particles have a spherical shape with a good dispersion. Less accumulation of nanoparticles was seen in Figure 2c, which may result from primary TiO$_2$ particles aggregating only at high calcination temperatures, which is essential to accelerate the crystal development of titanium dioxide in Figure 2c.[32] Adding g-C$_3$N$_4$ reduced the binary composite structure's sharp corners and edges, and as g-C$_3$N$_4$ surrounded the TiO$_2$/CdS composite, the nanoparticles were more concentrated on one another in Figure 2d.

The EDX technique was also employed to identify the elemental composition of the tested photocatalysts. Figure 3 shows EDX spectra of the individual and composite catalysts. This characterization method provides information about the elements present in each sample. Figure 3 shows the presence of Cd and S in the EDX spectrum of pure CdS. There were only two peaks showing nitrogen and carbon in the EDX spectrum of g-C$_3$N$_4$. Figure 3 also presents EDX spectrum of the CdS/TiO$_2$/g-C$_3$N$_4$ nanocomposite framework, demonstrating that the prepared nanocomposite comprises Cd, C, O, S, and Ti. The weight percentage of each sample in CdS, g-C$_3$N$_4$, TiO$_2$, and CdS/TiO$_2$/g-C$_3$N$_4$ is given in Table 1.

3.3. FTIR Analysis of Photocatalysts. FTIR patterns of the synthesized specimens are displayed in Figure 4. Four distinctive FTIR peaks for pure CdS were observed at 3355, 1630, 1407, and 1195 cm^{-1}. Moreover, the large absorption bands at wavenumbers of 3355 and 1630 cm^{-1} are assigned to stretching molecular vibrations of O−H bond of H$_2$O. Cd−S

bonds exhibit stretching vibrations due to a broad absorbance peak at 1195 cm^{-1}.[33] Three different absorption regions can be witnessed in pure g-C$_3$N$_4$, each at a wavenumber range of 3290−3063, 1627−1214, and 785 cm^{-1}. A broad absorbance band at 3290−3063 cm^{-1} is credited to stretching vibrations generated by NH$_2$ and N−H groups.[34] There are absorption peaks at 1627, 1576, 1400, 1309, and 1214 cm^{-1} in the FTIR spectrum of the g-C$_3$N$_4$ structure. These peaks are mostly generated by stretching vibrations of C−N heterocycles.[35] A clear, sharp peak corresponding to the g-C$_3$N$_4$ triazine unit stretching mode is seen at nearly 785 cm^{-1}.[19]

3.4. UV−vis DRS Study. Figure 5 reveals UV−vis patterns of CdS, g-C$_3$N$_4$, and TiO$_2$, as well as synthesized composite photocatalysts, including CdS/g-C$_3$N$_4$, TiO$_2$/g-C$_3$N$_4$, and CdS/TiO$_2$/g-C$_3$N$_4$. A semiconductor band structure is connected to its absorption area.[34] The pure CdS showed a shift in absorption wavelength toward longer wavelengths. Pure TiO$_2$ exhibits a basal absorption peak well below 370 nm, whereas g-C$_3$N$_4$ exhibits an absorption peak at around 460 nm. Using the relation described by Kubelka−Munk, the band gap of the specimens is estimated using Equation 2:

$$\alpha h\nu = A(h\nu - E_g)^2 \tag{2}$$

where A is a constant, h represents Planck's constant, ν denotes the frequency of light, d indicates the absorption coefficient, and E_g is the energy band gap. Since h is Planck's constant, ν represents the light frequency, and d is the absorption coefficient,[36] E_g values of 3.24, 2.6, 2.1, 2.68, 2.42, and 2.31 eV have been calculated for TiO$_2$, g-C$_3$N$_4$, CdS, CdS/g-C$_3$N$_4$,g-C$_3$N$_4$/TiO$_2$, and CdS/TiO$_2$/g-C$_3$N$_4$. A stronger photocatalytic activity is expected from the synthesized composite compared with pure semiconductors because of the improved optical response of the composite. The potential of VB edge (E_{VB}) and CB edge (E_{CB}) were measured using Equations 3 and (4):

$$E_{VB} = X - E^c + 0.5E_g \tag{3}$$

$$E_{CB} = E_{VB} - E_g \tag{4}$$

where X is the Mulliken electronegativity of the photocatalyst (5.81 eV for TiO$_2$, 5.18 eV for CdS, and 4.72 eV for g-C$_3$N$_4$), E^c is the free electron energy (4.5 eV vs NHE), and E_g is the band gap energy. The E_{VB} values of 2.93, 1.73, and 1.52 eV and E_{CB} values of −0.31, −0.37, and −1.08 eV were found for TiO$_2$, CdS, and g-C$_3$N$_4$ semiconductors, respectively.

3.5. Photocatalytic Efficiency Analysis. The dye solutions were irradiated with visible light to quantify the activity of the CdS, g-C$_3$N$_4$, TiO$_2$, and CdS/TiO$_2$/g-C$_3$N$_4$ samples. A UV−vis investigation was combined with a photocatalytic degradation reaction, including all catalysts, to examine the molecular modifications made to RhB dyes during the early phases of photocatalytic activity.[37] Figure 6 depicts the importance of the catalyst and light in the degradation process, where photolysis and catalysis demonstrated the lowest efficiency for RhB degradation. Within 180 min of visible light, the breakdown rate of RhB utilizing a TiO$_2$ catalyst reached 10%, but the photoactivity of CdS was insignificant.[38] This result demonstrated that CdS was inactive upon exposure to visible light. It was also hampered by the fast annihilation efficiency of the photoexcited charge carriers. The enhanced photodegradation performance of 99% within 180 min with CdS/TiO$_2$/g-C$_3$N$_4$ composite could be assigned to
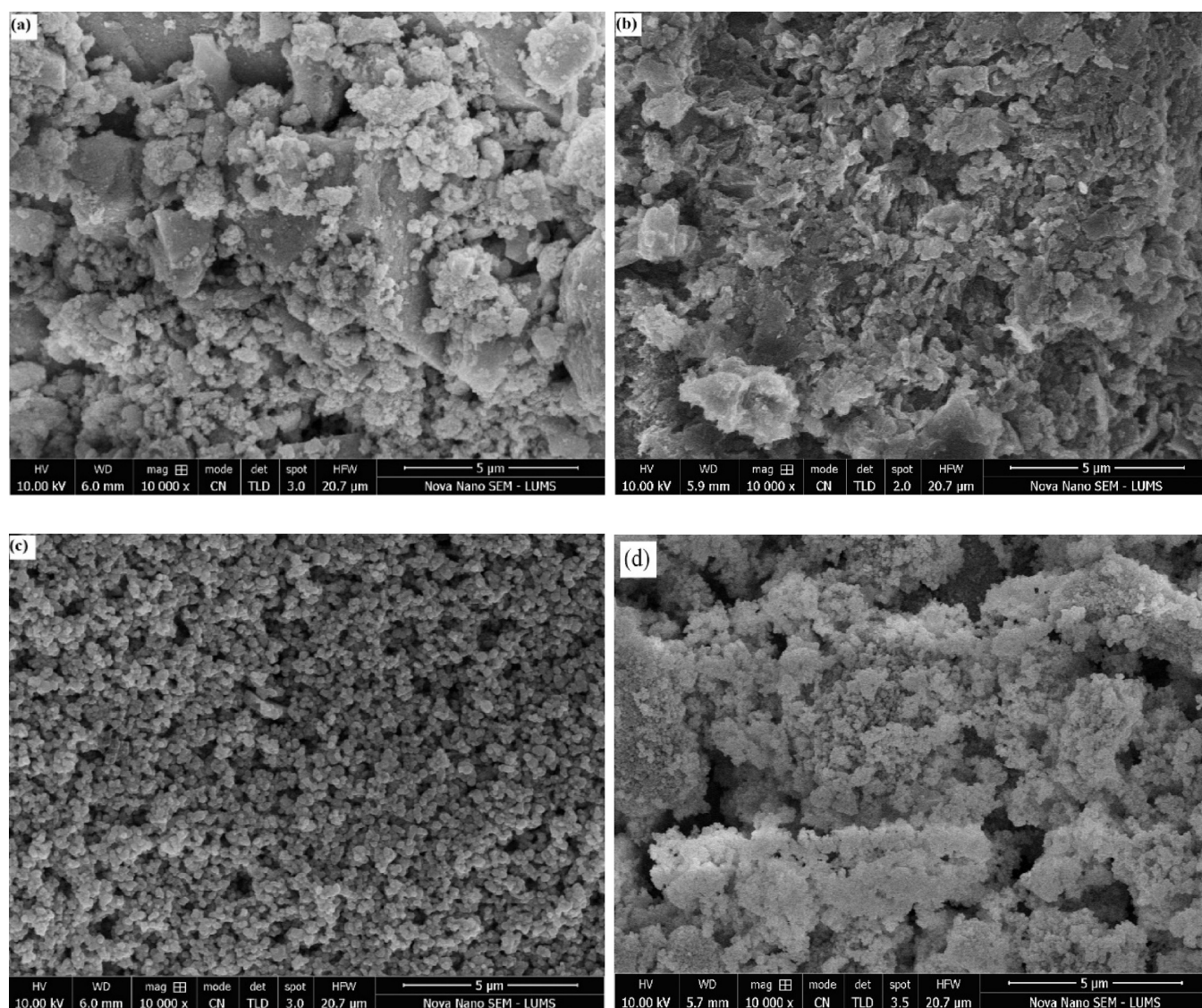
Figure 2. SEM micrographs of (a) CdS, (b) g-C$_3$N$_4$, (C) TiO$_2$, and (d) the CdS/TiO$_2$/g-C$_3$N$_4$ composite.

Table 1. Weight Percent of Constituent Elements of the Prepared Samples

element	CdS (wt %)	g-C$_3$N$_4$ (wt %)	TiO$_2$ (wt %)	CdS/TiO$_2$/g-C$_3$N$_4$ (wt %)
C		60.05		30.60
Cd	82.11			21.10
S	17.89			11.85
N		39.95		18.42
Ti			91.03	8.53
O			8.97	9.77
total %	100	100	100	100

TiO$_2$ acting as a conductive bridge between CdS and g-C$_3$N$_4$ and suppressing recombination of photoexcited charge carrier.[39] RhB has an initial concentration (C_0) at time 0 and final concentration (C) at time t of irradiation. Control experiments were conducted using RhB photodegradation without a catalyst. CdS/TiO$_2$/g-C$_3$N$_4$ completely degraded RhB after 180 min of UV irradiation. A kinetic curve of (C/C_0) against irradiation time (min) displays the degradation of the RhB dye using as-prepared catalysts. Equation 5 describes the reaction rate of RhB removal and the first order kinetics scheme fit to the experimental findings.

$$\ln(C_0/C) = kt \tag{5}$$

where k is a rate constant and C_0 and C represent the starting and final concentrations of RhB, respectively. According to Figure 7, photocatalysts were tested for pseudo-first-order kinetics to determine the RhB removal rate. Figure 7a shows the elimination of RhB using different photocatalysts, while Figure 7b shows a first-order kinetic model for RhB degradation.

The percentage degradation of RhB using different catalysts is shown in Figure 7(c). The maximum kinetic rate constant of 0.02701 min^{-1} was calculated for CdS/TiO$_2$/g-C$_3$N$_4$ composite catalyst, as showin in Figure 7(d). As demonstrated in Figure 7, pure CdS has a rate constant of 0.013 min^{-1}, TiO$_2$ has a rate constant of 0.0004 min^{-1}, and g-C$_3$N$_4$ has a rate constant of 0.0087 min^{-1}. The current study revealed that CdS/TiO$_2$/g-C$_3$N$_4$ k-value is by far the highest (0.0271 min^{-1}), which is almost 5.8 times, 3.1 times, and 2.1 times the rate constant of CdS, g-C$_3$N$_4$, and TiO$_2$, respectively.[40] The degradation rates for TiO$_2$, CdS, g-C$_3$N$_4$, CdS/g-C$_3$N$_4$ and g-
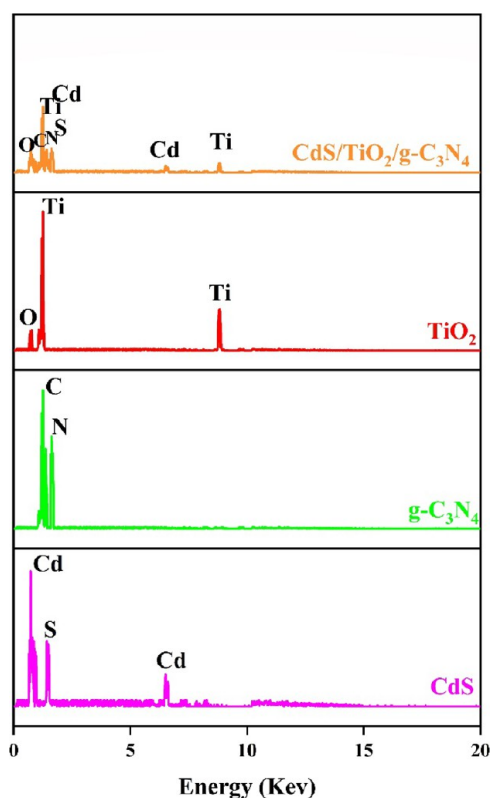
Figure 3. EDX analysis of (a) CdS; (b) g-C$_3$N$_4$; (c) TiO$_2$,; and (d) CdS/TiO$_2$/g-C$_3$N$_4$.
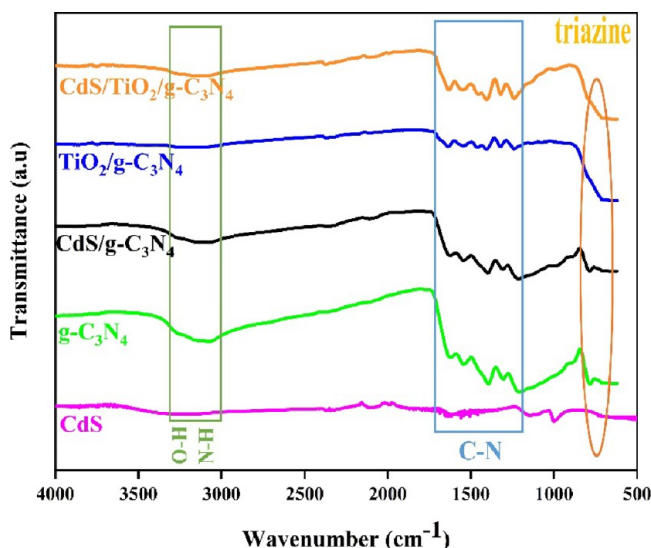
Figure 4. FTIR patterns of CdS, g-C$_3$N$_4$, CdS/g-C$_3$N$_4$, g-C$_3$N$_4$/TiO$_2$, and CdS/TiO$_2$/g-C$_3$N$_4$.

Figure 5. UV−vis profiles of CdS; g-C$_3$N$_4$; TiO$_2$; CdS/g-C$_3$N$_4$; g-C$_3$N$_4$/TiO$_2$, and CdS/TiO$_2$/g-C$_3$N$_4$.
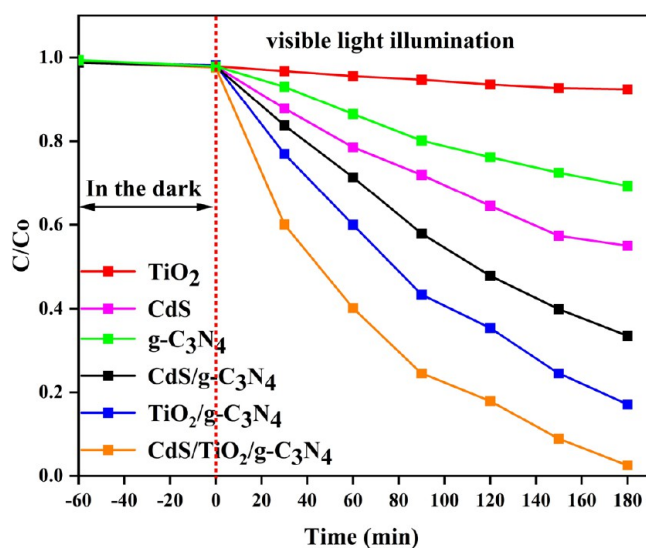
Figure 6. Photolysis and photocatalyst driven photodegradation of RhB.

C$_3$N$_4$/TiO$_2$ were calculated as 2%, 50.5%, 35.5%, 70.1%, 85.2%, and 99.4%, respectively.

3.6. Photocatalytic Hydrogen Production. The efficiency of the synthesized catalysts was probed by observing the evolution of H$_2$ from solution under light exposure. Figure 8a,b shows that H$_2$ yield after 5 h of exposure time reaches 300, 400, 600, 893, 1193, 1719, 2683, and 2910 μmol·h^{-1}·g^{-1} over P-25, CdS standard CdS, TiO$_2$, g-C$_3$N$_4$, CdS/g-C$_3$N$_4$, TiO$_2$/g-C$_3$N$_4$, and CdS/TiO$_2$/g-C$_3$N$_4$, respectively. The CdS/g-C$_3$N$_4$ and TiO$_2$/g-C$_3$N$_4$-initiated reactions yielded hydrogen pro-

duction rate of 1719 and 2683 μmol·h^{-1}·g^{-1}, respectively, which are much higher than those of pristine g-C$_3$N$_4$ and pure CdS. As anticipated, an outstanding hydrogen yield of 2910 μmol·h^{-1}·g^{-1} was possible with CdS/TiO$_2$/g-C$_3$N$_4$. As reported in Table 2, CdS/TiO$_2$/g-C$_3$N$_4$ produced hydrogen in a similar way to reported in previous research.[41−43] The apparent quantum yield (AQY) was checked at 420 and 480 nm wavelengths. The AQY of the CdS/TiO$_2$/g-C$_3$N$_4$ catalyst was relatively higher at 420 nm than 480 nm. At 420 nm, the AQY was 20%, which was reduced to 12% at 480 nm. Cao et al.[41] produced g-C$_3$N$_4$/CdS through the solvothermal rout and used for photocatalytic hydrogen production. They produced 37.45 μmol·h^{-1}·g^{-1} hydrogen under visible light irradiation. Similarly, Zhong et al.[42] used the hydrothermal method to produce g-C$_3$N$_4$/TiO$_2$ catalyst for hydrogen production experiments. They reported 126.4 μmol·h^{-1}·g^{-1} hydrogen in their work. Tonda et al.[43] used a facile wet-chemical route to produce g-C$_3$N$_4$(2D)/CdS (1D)/rGO dual-interface photocatalyst for hydrogen production under visible light. They
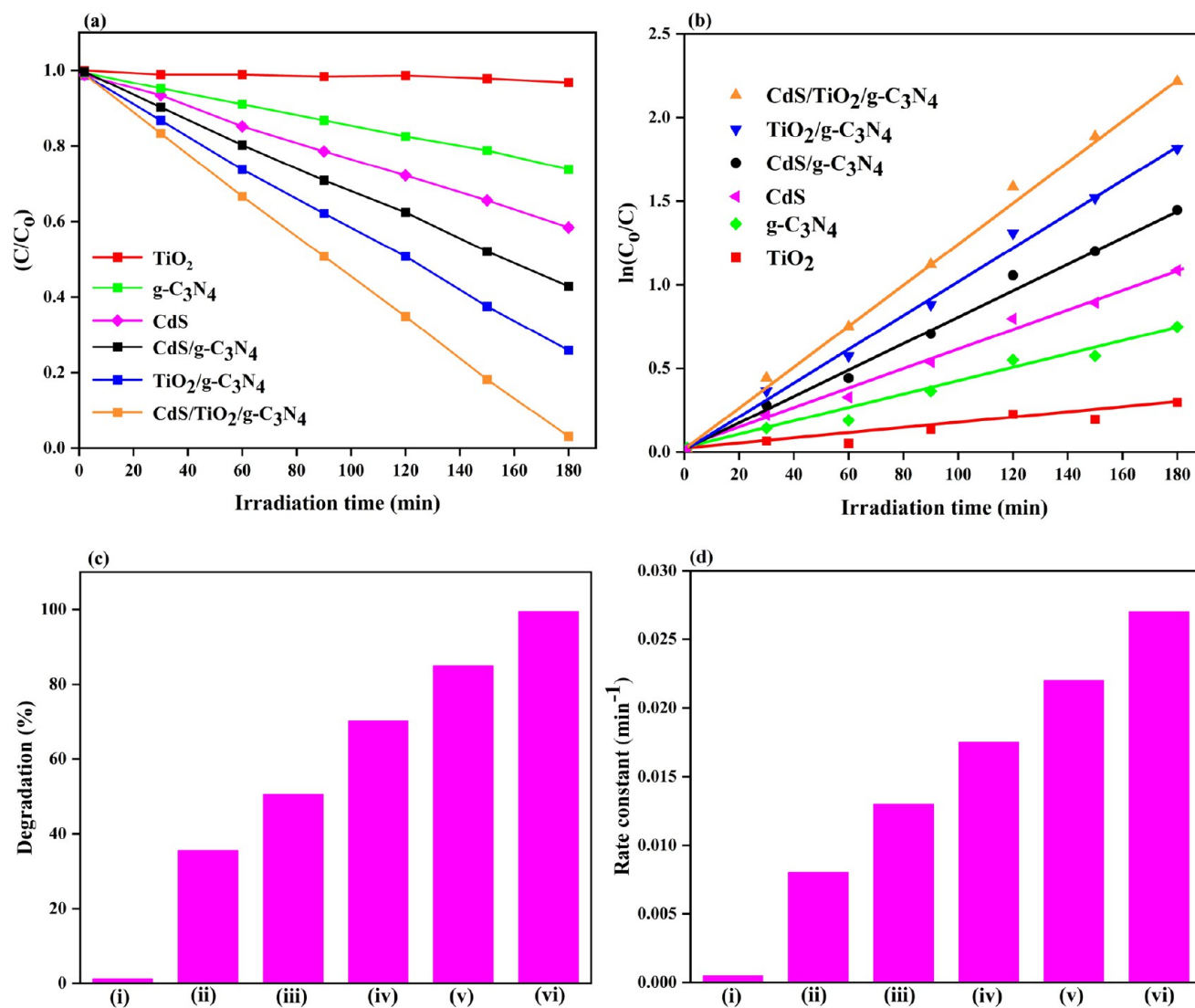
Figure 7. (a) Removal of RhB using different catalysts, (b) first-order kinetic model for RhB degradation, (c) degradation of RhB using (i) TiO$_2$, (ii) g-C$_3$N$_4$, (iii) CdS, (iv) CdS/g-C$_3$N$_4$, (v) g-C$_3$N$_4$/TiO$_2$ and (vi) TiO$_2$/CdS/g-C$_3$N$_4$, and (d) degradation rate constants of (i) TiO$_2$, (ii) g-C$_3$N$_4$, (iii) CdS, (iv) CdS/g-C$_3$N$_4$, (v) g-C$_3$N$_4$/TiO$_2$, and (vi) TiO$_2$/CdS/g-C$_3$N$_4$.
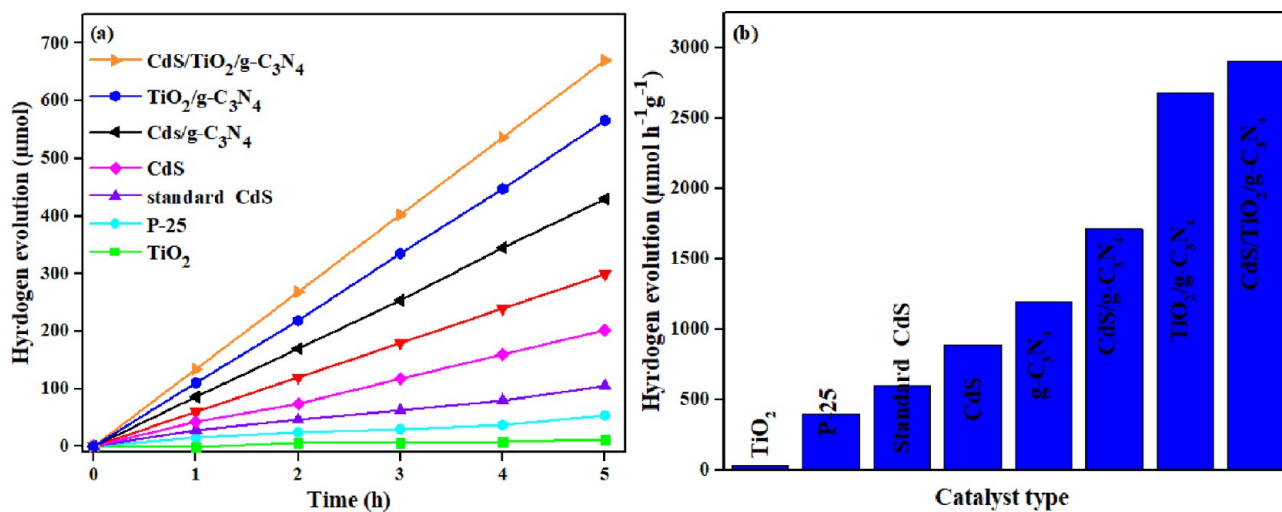

**Figure 8.** (a) Hydrogen evolution rate over time and (b) maximum hydrogen evolution over different catalysts.

Table 2. Comparison of Hydrogen Production Rates over Previously Reported Photocatalysts

photocatalyst	light source	preparation Method	H_2 (μmol·h^{-1}·g^{-1})	sacrificial agent	ref.
g-C$_3$N$_4$/CdS	300 W xenon lamp, visible light	solvothermal	37.45	C$_3$H$_8$O$_3$	41
g-C$_3$N$_4$/TiO$_2$	300 W xenon lamp, UV-light	hydrothermal	126.4	Na$_2$S/NaSO$_3$	42
g-C$_3$N$_4$/CdS/Rgo	300 W Xe arc lamp, visible light	facile wet-chemical	1982.7	Na$_2$S/NaSO$_3$	43
CdS/g-C$_3$N$_4$/ZnFe$_2$O$_4$	300 W Xe lamp, visible light	ultrasonically assisted synthesis	1315.2	TEOA	44
CdS/ZnFe$_2$O$_4$/Cu$_2$O	300 W Xe lamp, visible light	hydrothermal	1877.3	C$_3$H$_8$O$_3$	45
CdS/TiO$_2$/g-C$_3$N$_4$	300 W Xe lamp, visible light	hydrothermal	2910.1	Na$_2$S/NaSO$_3$	this study

reported a relatively higher hydrogen evolution of 1982.7 μmol·h^{-1}·g^{-1} under visible light exposure. Belakehal et al.[44] tested CdS/g-C$_3$N$_4$/ZnFe$_2$O$_4$ to produce hydrogen and reported a maximum evolution rate of 1315.2 μmol·h^{-1}·g^{-1}. Yao et al.[45] used a hydrothermal method to produce CdS/ZnFe$_2$O$_4$/Cu$_2$O photocatalyst. They replaced Cu$_2$O with g-C$_3$N$_4$ in the formulation reported by Belakehal et al.[44] and found a significant increase in the hydrogen evolution under similar conditions (877.3 μmol·h^{-1}·g^{-1}). In the current study, a common hydrothermal method was used to produce the CdS/TiO$_2$/g-C$_3$N$_4$ composite photocatalyst. This photocatalyst resulted in a high hydrogen evolution rate of 2910.1 μmol·h^{-1}·g^{-1} among the above-reported works.

3.7. CdS/TiO$_2$/g-C$_3$N$_4$ Photocatalysis Mechanism. The hydrogen evolution rate also varies with sacrificial reagent systems.[46] The photocatalytic processes employing pure water are usually inefficient. Pure water undergoes reduction and oxidation reactions simultaneously, which is a difficult multistep process requiring four electrons to complete the reaction.[47] Utilizing scavenger molecules as electron donors can dramatically boost H$_2$ generation, since they scavenge holes and significantly lower charge carrier recombination. Since O$_2$ is not produced, a subsequent gas separation stage is also avoided, which also inhibits the reverse reaction that would normally produce water and boosts the H$_2$ output. The hydrogen production rate in the Na$_2$S/Na$_2$SO$_3$ combination is more significant than in systems using lactic acid, triethanolamine (TEOA), and ethanol as sacrificial agents. It is ascribed to the capability of Na$_2$S/Na$_2$SO$_3$ to consume holes and safeguard CdS rapidly.[48] The amount of photocatalysts utilized in the hydrogen evolution test is also a significant component that influences the hydrogen evolution rate, and 10 mg is the ideal amount for this work. CdS/TiO$_2$/g-C$_3$N$_4$ hydrogen evolution at an optimal rate of 2910 μmol·g^{-1}·h^{-1}, is much higher than the evolution rate over CdS. Effectively consuming the photogenerated holes, the sacrificial agent also prevents CdS from oxidizing. The most often utilized sacrificial agents for CdS-based photocatalytic processes are mixed aqueous solutions of S^{2-} and SO$_3^{2-}$. The holes in the valence band of Na$_2$S/Na$_2$SO$_3$ sacrificial agent oxidize S^{2-} and SO$_3^{2-}$ to yield S$_2^{2-}$ and SO$_4^{2-}$, respectively.[48] The sacrificial agent would not be completely consumed before the holes would begin to oxidize the CdS. The SO$_3^{2-}$ ion in the solution will first interact with the S$_2^{2-}$ ion to create S^{2-} and S$_2$O$_3^{2-}$, even though the ensuing S$_2^{2-}$ will prevent the photocatalyst from absorbing light. The S^{2-} ions prevent defects from forming on CdS, although the colorless S$_2$O$_3^{2-}$ has no adverse effects on the light absorption activity of CdS. Under the protection of an S^{2-} and SO$_3^{2-}$ mixed solution, CdS can remain reasonably stable during H$_2$ generation. The sacrificial agents S^{2-} and SO$_3^{2-}$ entirely transform into S$_2$O$_3^{2-}$ as the reaction progresses. When CdS can no longer be protected, its ability to produce H$_2$ starts to deteriorate.

tert-Butanol (TBA), 1,4-benzoquinone (BQ), and Triethanolamine (TEOA) were evaluated as different trapping reagents in radical trapping research of the photodegradation activities over CdS/TiO$_2$/g-C$_3$N$_4$ for eliminating h$^+$, · OH, and ·O$_2^-$, as shown in Figure 9. Trapping tests revealed that TBA
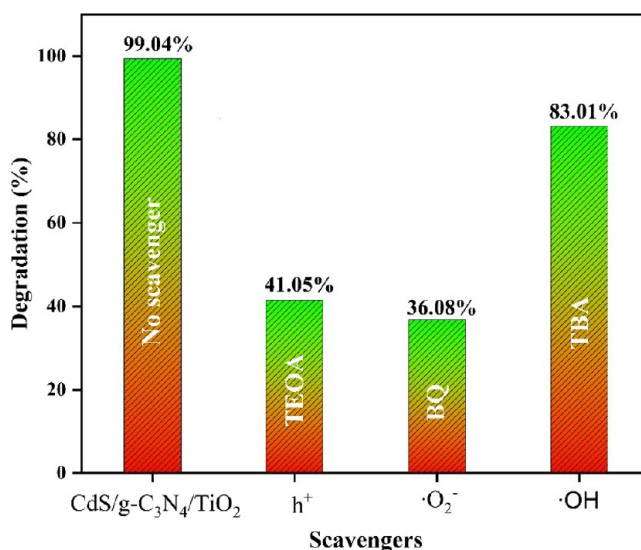
Figure 9. Radical capturing by the CdS/TiO$_2$/g-C$_3$N$_4$ composite.

was not the primary scavenger in the photodegradation, demonstrating that hydroxyl ions were not the primary active charge carriers in photocatalytic activity.[49] A significant decrease in the photocatalytic efficiency occurs when TEOA is used as an acceptor. This indicates that h$^+$ is crucial to the photocatalytic process. When BQ is added to RhB aqueous solution, containing CdS/TiO$_2$/g-C$_3$N$_4$, significant reductions are observed in its photodegradation performance. In the aqueous phase, illuminated by visible light, O^{2-} and h$^+$ seem to be the major species that participate in the photocatalytic degradation of RhB.[50]

The band gaps of CdS, TiO$_2$, and g-C$_3$N$_4$ were 2.1, 3.24, and 2.60 eV, respectively. Under visible light, the holes and electrons were produced in their respective VB and CB. The CdS, TiO$_2$, and g-C$_3$N$_4$ possessed E_{CB} potentials of −0.37, −0.31, and −1.08 eV, respectively. Similarly, the E_{VB} potential was measured as 1.73, 2.93, and 1.62 eV, respectively, as shown in Figure 10. The potential of the band edges of the three components reveals that the possible charge transfer mechanism over CdS/TiO$_2$/g-C$_3$N$_4$ is the S-scheme. The CB potential of g-C$_3$N$_4$ was the most favorable for the reduction reaction, whereas the VB potential of TiO$_2$ was more probable for the oxidation reaction. As a consequence of suitable band arrangements in CdS, TiO$_2$, and g-C$_3$N$_4$, the photogenerated electrons at the CB of TiO$_2$ with the relatively weakest reduction potential could easily recombine and annihilate with
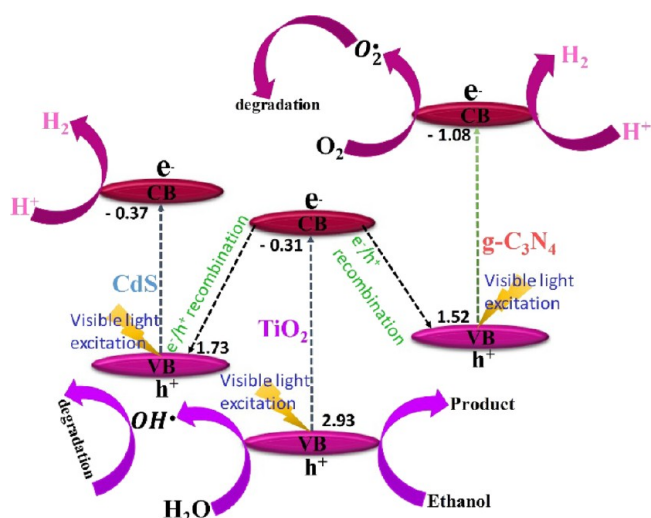
Figure 10. Schematic of photocatalytic mechanism of CdS/TiO₂/g-₃N₄ heterojunction.

photogenerated holes having relatively low oxidation potentials at the VB of CdS and g-C₃N₄ through closely connected interfaces.[51]

As a result, the photogenerated electrons of strong reduction potential survived at the CB of CdS and g-C₃N₄, and photoexcited holes of powerful oxidation potential remained unutilized at the VB of TiO₂.[52] Hence, the CB of TiO₂ can immediately transfer electrons to the VB of CdS and g-C₃N₄ in the heterojunctions through closely connected interfaces, and the photogenerated electrons at the CB of CdS and g-C₃N₄ and holes at the VB of TiO₂ are utilized in the redox reactions. The photoexcited electrons can interact with the O_2 in CBs of g-C₃N₄ and CdS to produce $\bullet O_2$, whereas photogenerated holes at the VB of TiO₂ possessed sufficient oxidation potential to oxidize OH^- to $\bullet OH$. Subsequently, these redox species ($\bullet OH$, $\bullet O_2$) degraded the pollutants. For H_2 evolution, the photoexcited electrons at the CB of CdS and g-C₃N₄ reduce the H^+ ions to produce H_2, whereas the sacrificial reagent scavenged the holes at the VB of TiO₂.

In summary, the photocatalytic mechanism of the CdS/TiO₂/g-C₃N₄ heterostructure involves the synergy of multiple semiconductors to enhance the photocatalytic activity. The
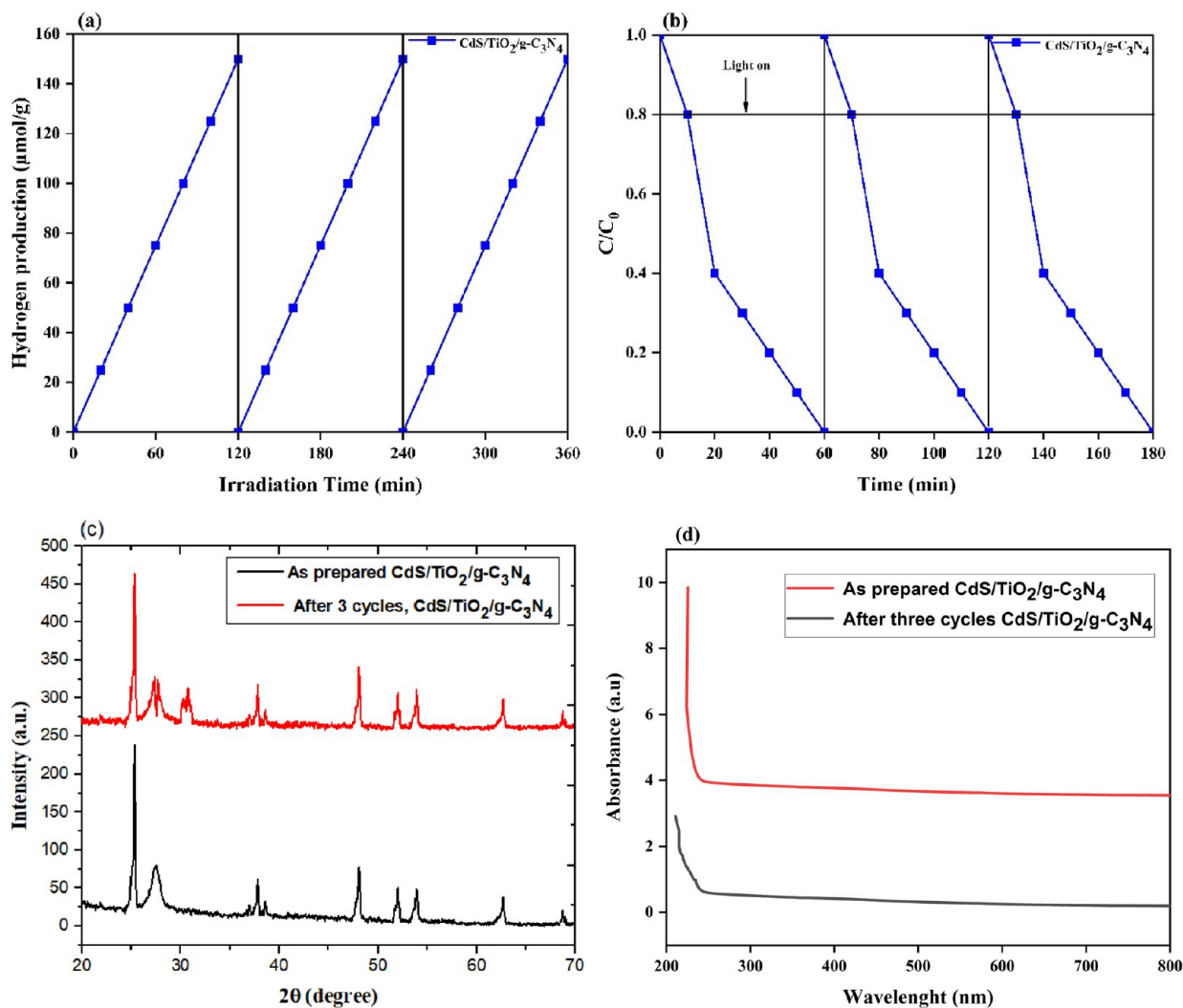

Figure 11. Cycle performance of CdS/TiO₂/g-C₃N₄ for the production of hydrogen: (a) photodegradation of RhB, (b) spectrographs of the CdS/TiO₂/g-C₃N₄ photocatalyst after 3 cycles of RhB degradation, (c) XRD of the before and after photocatalytic experiments, and (d) UV–vis absorption before and after photocatalytic experiments.

electrons in the CB of CdS migrate to the CB of TiO_2 by creating a flow of electrons. The electron transfer process causes the formation of superoxide radicals due to the reduction of TiO_2. The hole left behind in the VB of CdS simultaneously migrates to the VB of $g-C_3N_4$ due to the alignment of their energy levels. The flow of holes contributes to the oxidation of water or organic pollutants. The superoxide radical TiO_2 surface and the holes on $g-C_3N_4$ react with water or organic pollutants adsorbed on the photocatalyst surface. These reactions lead to the formation of hydroxyl radicals and other reactive oxygen species (ROS), which are highly oxidative toward the degradation of pollutants. The photo-generated hydroxyl radicals and ROS attack and oxidize organic molecules into less harmful compounds. Under certain conditions, electron–hole pairs reduce protons from water into molecular hydrogen.

3.8. Recyclability Examination. The recyclability of any photocatalyst is an important factor in determining its practical application. The $CdS/TiO_2/g-C_3N_4$ displayed good photo-catalytic H_2 evolution and RhB degradation efficiencies, as shown in Figure 11a,b. The photocatalytic activity of this catalyst remained sustained after three irradiation cycles. This demonstrates that the ternary composite material can be used repeatedly without losing photocatalytic effectiveness. In addition, a synergistic effect between CdS, $g-C_3N_4$, and TiO_2 leads to the excellent photocorrosion resistance of $g-C_3N_4$. Furthermore, $g-C_3N_4$ performs an essential function as a shield, protecting inorganic semiconductor components and sacrificial agents from attack by excess hydroxyl groups, thus allowing for longer utilization times of semiconductors. Using XRD and UV–vis absorption tests, characterization tests of $CdS/TiO_2/g-C_3N_4$ were conducted after three cycles and compared with the designs before irradiation, as illustrated in Figure 11c,d. The $CdS/TiO_2/g-C_3N_4$ photocatalyst showed a very high level of stability. It was found that there was no significant difference between the catalyst structure before and after use in terms of its structure.

4. CONCLUSIONS

The photocatalytic effectiveness of the synthesized materials was checked by tracking the evolution of hydrogen from solution under exposure to light. The hydrogen production reached 300, 400, 600, 893, 1193, 1719, 2683, and 2910 $\mu mol\cdot h^{-1}\cdot g^{-1}$ over P-25, CdS standard CdS, TiO_2, $g-C_3N_4$, CdS/g-C_3N_4, $TiO_2/g-C_3N_4$, and $CdS/TiO_2/g-C_3N_4$, respectively. A high hydrogen yield of 2910 $\mu mol\cdot h^{-1}\cdot g^{-1}$ was possible with the $CdS/TiO_2/g-C_3N_4$ photocatalyst. Experimental findings demonstrated photocatalytic degradation efficiency for Rhod-amine B up to 99.4%, which is much higher than all other tested composites. The maximum kinetic rate constant value of 0.02701 min^{-1} was discovered for the $CdS/TiO_2/g-C_3N_4$ composite catalyst. The pure CdS has a rate constant of 0.013 min^{-1}, TiO_2 has a rate constant of 0.0004 min^{-1}, and g-C_3N_4 has a rate constant of 0.0087 min^{-1}. The hydrogen production rate in the Na_2S/Na_2SO_3 combination was more effective than that in systems using lactic acid, triethanolamine, and ethanol as sacrificial agents. It is ascribed to the capability of Na_2S/Na_2SO_3 to consume holes and safeguard CdS rapidly.

■ AUTHOR INFORMATION

Corresponding Author

Shazia Shukrullah − *Department of Physics, University of Agriculture Faisalabad, Faisalabad 38040, Pakistan;* orcid.org/0000-0002-4474-3768; Email: zshukrullah@gmail.com

Authors

Muhammad Shoaib − *Department of Physics, University of Agriculture Faisalabad, Faisalabad 38040, Pakistan*

Muhammad Yasin Naz − *Department of Physics, University of Agriculture Faisalabad, Faisalabad 38040, Pakistan;* orcid.org/0000-0002-8490-7819

Muhammad Adnan Munir − *Department of Physics, University of Agriculture Faisalabad, Faisalabad 38040, Pakistan*

Muhammad Irfan − *Electrical Engineering Department, College of Engineering, Najran University Saudi Arabia, Najran 61441, Saudi Arabia;* orcid.org/0000-0003-4161-6875

Saifur Rahman − *Electrical Engineering Department, College of Engineering, Najran University Saudi Arabia, Najran 61441, Saudi Arabia*

Abdulnoor Ali Jazem Ghanim − *Civil Engineering Department, College of Engineering, Najran University, Najran 61441, Saudi Arabia*

Complete contact information is available at:
https://pubs.acs.org/10.1021/acsomega.3c06759

Notes

The authors declare no competing financial interest.

■ ACKNOWLEDGMENTS

■ REFERENCES

(1) Antony, R. P.; Mathews, T.; Ramesh, C.; Murugesan, N.; Dasgupta, A.; Dhara, S.; Dash, S.; Tyagi, A. Efficient photocatalytic hydrogen generation by Pt modified TiO_2 nanotubes fabricated by rapid breakdown anodization. *Int. J. Hydrogen Energy* **2012**, *37* (10), 8268−8276.

(2) Tran, P. D.; Batabyal, S. K.; Pramana, S. S.; Barber, J.; Wong, L. H.; Loo, S. C. J. A cuprous oxide−reduced graphene oxide (Cu_2O−rGO) composite photocatalyst for hydrogen generation: employing rGO as an electron acceptor to enhance the photocatalytic activity and stability of Cu_2O. *Nanoscale* **2012**, *4* (13), 3875−3878.

(3) Ouyang, S.; Tong, H.; Umezawa, N.; Cao, J.; Li, P.; Bi, Y.; Zhang, Y.; Ye, J. Surface-alkalinization-induced enhancement of photocatalytic H_2 evolution over $SrTiO_3$-based photocatalysts. *J. Am. Chem. Soc.* **2012**, *134* (4), 1974−1977.

(4) Lv, H.; Ma, L.; Zeng, P.; Ke, D.; Peng, T. Synthesis of floriated $ZnFe_2O_4$ with porous nanorod structures and its photocatalytic hydrogen production under visible light. *J. Mater. Chem.* **2010**, *20* (18), 3665−3672.

(5) Girginer, B.; Galli, G.; Chiellini, E.; Bicak, N. Preparation of stable CdS nanoparticles in aqueous medium and their hydrogen generation efficiencies in photolysis of water. *Int. J. Hydrogen Energy* **2009**, *34* (3), 1176−1184.

(6) Cao, S. W.; Fang, J.; Shahjamali, M. M.; Boey, F. Y.; Barber, J.; Loo, S. C. J.; Xue, C. Plasmon-enhanced hydrogen evolution on Au-$InVO_4$ hybrid microspheres. *RSC Adv.* **2012**, *2* (13), 5513−5515.

(7) White, J. L.; Baruch, M. F.; Pander, J. E., III; Hu, Y.; Fortmeyer, I. C.; Park, J. E.; Zhang, T.; Liao, K.; Gu, J.; Yan, Y.; Shaw, T. W.; Abelev, E.; Bocarsly, A. B. Light-driven heterogeneous reduction of carbon dioxide: photocatalysts and photoelectrodes. *Chem. Rev.* **2015**, *115*, 12888.

(8) Fu, S.; Yuan, W.; Yan, Y.; Liu, H.; Shi, X.; Zhao, F.; Zhou, J. Highly efficient visible-light photoactivity of Z-scheme MoS_2/Ag_2CO_3 photocatalysts for organic pollutants degradation and bacterial inactivation. *Journal of Environmental Management* **2019**, *252*, No. 109654.

(9) Shen, H.; Peppel, T.; Strunk, J.; Sun, Z. Photocatalytic reduction of CO_2 by metal-free-based materials: recent advances and future perspective. *Solar RRL* **2020**, *4* (8), 1900546.

(10) Doan, V. D.; Huynh, B. A.; Pham, H. A. L.; Vasseghian, Y.; Le, V. T. Cu_2O/Fe_3O_4/MIL-101 (Fe) nanocomposite as a highly efficient and recyclable visible-light-driven catalyst for degradation of ciprofloxacin. *Environ. Res.* **2021**, *201*, No. 111593.

(11) Moradi, M.; Vasseghian, Y.; Khataee, A.; Harati, M.; Arfaeinia, H. Ultrasound-assisted synthesis of $FeTiO_3$/GO nanocomposite for photocatalytic degradation of phenol under visible light irradiation. *Sep. Purif. Technol.* **2021**, *261*, No. 118274.

(12) Jin, Z.; Wang, X.; Hao, X.; Wang, G.; Guo, X.; Wang, K. Graphdiyne based GDY/CuI/NiO parallel double S-scheme heterojunction for efficient photocatalytic hydrogen evolution. *2D Materials* **2022**, *9* (2), No. 025014.

(13) Elavarasan, N.; Vignesh, S.; Srinivasan, M.; Venkatesh, G.; Palanisamy, G.; Ramasamy, P.; Palanivel, B.; Al-Enizi, A. M.; Ubaidullah, M.; Minnam Reddy, V. R.; Kim, W. K. Synergistic S-Scheme mechanism insights of g-C_3N_4 and rGO combined ZnO-Ag heterostructure nanocomposite for efficient photocatalytic and anticancer activities. *J. Alloys Compd.* **2022**, *906*, No. 164255.

(14) Jin, Z.; Jiang, X.; Guo, X. Hollow tubular Co9S8 grown on In_2O_3 to form S-scheme heterojunction for efficient and stable hydrogen evolution. *Int. J. Hydrogen Energy* **2022**, *47* (3), 1669−1682.

(15) Li, B.; Zhang, B.; Zhang, Y.; Zhang, M.; Huang, W.; Yu, C.; Sun, J.; Feng, J.; Dong, S.; Sun, J. Porous g-C_3N_4/TiO_2 S-scheme heterojunction photocatalyst for visible-light driven H_2-production and simultaneous wastewater purification. *Int. J. Hydrogen Energy* **2021**, *46* (64), 32413−32424.

(16) Shi, J.; Zheng, B.; Mao, L.; Cheng, C.; Hu, Y.; Wang, H.; Li, G.; Jing, D.; Liang, X. MoO_3/g-C3N4 Z-scheme (S-scheme) system derived from MoS_2/melamine dual precursors for enhanced photocatalytic H_2 evolution driven by visible light. *Int. J. Hydrogen Energy* **2021**, *46* (3), 2927−2935.

(17) Xu, Q.; Zhang, L.; Cheng, B.; Fan, J.; Yu, J. S-Scheme Heterojunction Photocatalyst. *Chem.* **2020**, *6* (7), 1543−1559.

(18) Zhu, C.; Liu, C. a.; Fu, Y.; Gao, J.; Huang, H.; Liu, Y.; Kang, Z. Construction of CDs/CdS photocatalysts for stable and efficient hydrogen production in water and seawater. *Applied Catalysis B: Environmental* **2019**, *242*, 178−185.

(19) Chen, F.; Jin, X.; Jia, D.; Cao, Y.; Duan, H.; Long, M. Efficient treament of organic pollutants over CdS/graphene composites photocatalysts. *Appl. Surf. Sci.* **2020**, *504*, No. 144422.

(20) Cui, Y.; Tang, Y.; Wang, X. Template-free synthesis of graphitic carbon nitride hollow spheres for photocatalytic degradation of organic pollutants. *Mater. Lett.* **2015**, *161*, 197−200.

(21) Zhu, J.; Xiao, P.; Li, H.; Carabineiro, S. A. Graphitic carbon nitride: synthesis, properties, and applications in catalysis. *ACS Appl. Mater. Interfaces* **2014**, *6* (19), 16449−16465.

(22) Hu, S.; Li, F.; Fan, Z.; Wang, F.; Zhao, Y.; Lv, Z. Band gap-tunable potassium doped graphitic carbon nitride with enhanced mineralization ability. *Dalton Transactions* **2015**, *44* (3), 1084−1092.

(23) Zhou, L.; Zhang, H.; Guo, X.; Sun, H.; Liu, S.; Tade, M. O.; Wang, S. Metal-free hybrids of graphitic carbon nitride and nanodiamonds for photoelectrochemical and photocatalytic applications. *J. Colloid Interface Sci.* **2017**, *493*, 275−280.

(24) Ding, M.; Wang, W.; Zhou, Y.; Lu, C.; Ni, Y.; Xu, Z. Facile in situ synthesis of 2D porous g-C_3N_4 and g-C_3N_4/P_{25} (N) heterojunction with enhanced quantum effect for efficient photocatalytic application. *J. Alloys Compd.* **2015**, *635*, 34−40.

(25) Wang, K.; Li, Q.; Liu, B.; Cheng, B.; Ho, W.; Yu, J. Sulfur-doped g-C_3N_4 with enhanced photocatalytic CO_2-reduction performance. *Applied Catalysis B: Environmental* **2015**, *176*, 44−52.

(26) Sharma, M.; Vaidya, S.; Ganguli, A. K. Enhanced photocatalytic activity of g-C_3N_4-TiO_2 nanocomposites for degradation of Rhodamine B dye. *J. Photochem. Photobiol., A* **2017**, *335*, 287−293.

(27) Atacan, K.; Özacar, M. Construction of a non-enzymatic electrochemical sensor based on CuO/g-C3N4 composite for selective detection of hydrogen peroxide. *Mater. Chem. Phys.* **2021**, *266*, No. 124527.

(28) Hashem, E. M.; Hamza, M. A.; El-Shazly, A. N.; Abd El-Rahman, S. A.; El-Tanany, E. M.; Mohamed, R. T.; Allam, N. K. Novel Z-Scheme/Type-II CdS@ ZnO/g-C_3N_4 ternary nanocomposites for the durable photodegradation of organics: kinetic and mechanistic insights. *Chemosphere* **2021**, *277*, No. 128730.

(29) Liu, X.; Sayed, M.; Bie, C.; Cheng, B.; Hu, B.; Yu, J.; Zhang, L. Hollow CdS-based photocatalysts. *Journal of Materiomics* **2021**, *7* (3), 419−439.

(30) Renukadevi, S.; Jeyakumari, A. P. Rational design of $ZnFe_2O_4$/g-C_3N_4 heterostructures composites for high efficient visible-light photocatalysis for degradation of aqueous organic pollutants. *Inorg. Chem. Commun.* **2020**, *118*, No. 108047.

(31) Wang, J.; Yu, L.; Wang, Z.; Wei, W.; Wang, K.; Wei, X. Constructing 0D/2D Z-Scheme Heterojunction of CdS/g-C_3N_4 with Enhanced Photocatalytic Activity for H_2 Evolution. *Catal. Lett.* **2021**, *151* (12), 3550−3561.

(32) Chen, Y. F.; Lee, C. Y.; Yeng, M. Y.; Chiu, H. T. The effect of calcination temperature on the crystallinity of TiO_2 nanopowders. *J. Cryst. Growth* **2003**, *247* (3−4), 363−370.

(33) Fu, J.; Chang, B.; Tian, Y.; Xi, F.; Dong, X. Novel C_3N_4−CdS composite photocatalysts with organic−inorganic heterojunctions: in situ synthesis, exceptional activity, high stability and photocatalytic mechanism. *Journal of Materials Chemistry A* **2013**, *1* (9), 3083−3090.

(34) Jiang, F.; Yan, T.; Chen, H.; Sun, A.; Xu, C.; Wang, X. A g-C_3N_4−CdS composite catalyst with high visible-light-driven catalytic activity and photostability for methylene blue degradation. *Appl. Surf. Sci.* **2014**, *295*, 164−172.

(35) Yan, S.; Li, Z.; Zou, Z. Photodegradation performance of g-C_3N_4 fabricated by directly heating melamine. *Langmuir* **2009**, *25* (17), 10397−10401.

(36) Chen, Y.; Huang, W.; He, D.; Situ, Y.; Huang, H. Construction of heterostructured g-C_3N_4/Ag/TiO_2 microspheres with enhanced photocatalysis performance under visible-light irradiation. *ACS Appl. Mater. Interfaces* **2014**, *6* (16), 14405−14414.

(37) Fu, J.; Xu, Q.; Low, J.; Jiang, C.; Yu, J. Ultrathin 2D/2D WO_3/g-C_3N_4 step-scheme H_2-production photocatalyst. *Applied Catalysis B: Environmental* **2019**, *243*, 556−565.

(38) Udayabhanu; Lakshmana Reddy, N.; Shankar, M. V.; Sharma, S. C.; Nagaraju, G. One-pot synthesis of Cu−TiO_2/CuO nanocomposite: application to photocatalysis for enhanced H_2 production, dye degradation & detoxification of Cr (VI). *Int. J. Hydrogen Energy* **2020**, *45* (13), 7813−7828.

(39) Shoaib, M.; Naz, M. Y.; Shukrullah, S.; Munir, M. A.; Ghaffar, A.; Irfan, M.; Mursal, S. N. F.; Kamran, K. Synthesis and testing of photocatalytic potential of $MgFe_2O_4$/ZnO/perlite magnetic heterojunction for degradation of synthetic dyes. *Appl. Phys. A: Mater. Sci. Process.* **2022**, *128* (11), 979.

(40) Shoaib, M.; Munir, M. A.; Naz, M. Y.; Abbas, G.; Irfan, M.; Rahman, S.; Ghanim, A. A. J. Testing of Magnetic ZnO/$MgFe_2O_4$ Heterostructures for Photocatalytic Removal of Synthetic Dye Pollutants from Wastewater. *Water, Air, & Soil Pollution* **2023**, *234* (7), 422.

(41) Cao, S. W.; Yuan, Y. P.; Fang, J.; Shahjamali, M. M.; Boey, F. Y. C.; Barber, J.; Loo, S. C. J.; Xue, C. In-situ growth of CdS quantum dots on g-C_3N_4 nanosheets for highly efficient photocatalytic hydrogen generation under visible light irradiation. *Int. J. Hydrogen Energy* **2013**, *38* (3), 1258−1266.

(42) Zhong, X.; Jin, M.; Dong, H.; Liu, L.; Wang, L.; Yu, H.; Leng, S.; Zhuang, G.; Li, X.; Wang, J. G. TiO_2 nanobelts with a uniform coating of g-C_3N_4 as a highly effective heterostructure for enhanced photocatalytic activities. *J. Solid State Chem.* **2014**, *220*, 54−59.

(43) Tonda, S.; Kumar, S.; Gawli, Y.; Bhardwaj, M.; Ogale, S. g-C_3N_4 (2D)/CdS (1D)/rGO (2D) dual-interface nano-composite for excellent and stable visible light photocatalytic hydrogen generation. *Int. J. Hydrogen Energy* **2017**, *42* (9), 5971−5984.

(44) Belakehal, R.; Atacan, K.; Güy, N.; Megriche, A.; Özacar, M. Fabrication of heterostructured CdS/g-C_3N_4/$ZnFe_2O_4$ nanocomposite synthesized through ultrasonic-assisted method for efficient photocatalytic hydrogen production. *Appl. Surf. Sci.* **2022**, *602*, No. 154315.

(45) Yao, L.; Wang, W.; Zhu, T.; Wang, Y.; Liang, Y.; Fu, J.; Wang, J.; Cheng, Y.; Liu, S. A rational design of CdS/$ZnFe_2O_4$/Cu_2O core-shell nanorod array photoanode with stair-like type-II band alignment for highly efficient bias-free visible-light-driven H2 generation. *Applied Catalysis B: Environmental* **2020**, *268*, No. 118460.

(46) Kawai, T.; Sakata, T. Photocatalytic hydrogen production from liquid methanol and water. *J. Chem. Soc., Chem. Commun.* **1980**, *15*, 694−695.

(47) Schneider, J.; Bahnemann, D. W. Undesired Role of Sacrificial Reagents in Photocatalysis. *J. Phys. Chem. Lett.* **2013**, *4* (20), 3479−3483.

(48) Li, Q.; Li, X.; Yu, J. Chapter 10 - Surface and interface modification strategies of CdS-based photocatalysts. In *Interface Science and Technology*, Yu, J., Jaroniec, M., Jiang, C., Eds.; Vol. *31*; Elsevier, 2020; pp 313−348 DOI: 10.1016/B978-0-08-102890-2.00010-5.

(49) Li, F. T.; Wang, Q.; Ran, J.; Hao, Y. J.; Wang, X. J.; Zhao, D.; Qiao, S. Z. Ionic liquid self-combustion synthesis of BiOBr/$Bi_{24}O_{31}Br_{10}$ heterojunctions with exceptional visible-light photocatalytic performances. *Nanoscale* **2015**, *7* (3), 1116−1126.

(50) Yuan, H.; Shi, W.; Lu, J.; Wang, J.; Shi, Y.; Guo, F.; Kang, Z. Dual-channels separated mechanism of photo-generated charges over semiconductor photocatalyst for hydrogen evolution: Interfacial charge transfer and transport dynamics insight. *Chemical Engineering Journal* **2023**, *454*, No. 140442.

(51) Shi, W.; Ren, H.; Huang, X.; Li, M.; Tang, Y.; Guo, F. Low cost red mud modified graphitic carbon nitride for the removal of organic pollutants in wastewater by the synergistic effect of adsorption and photocatalysis. *Sep. Purif. Technol.* **2020**, *237*, No. 116477.

(52) Shi, W.; Cao, L.; Shi, Y.; Chen, Z.; Cai, Y.; Guo, F.; Du, X. Environmentally friendly supermolecule self-assembly preparation of S-doped hollow porous tubular g-C_3N_4 for boosted photocatalytic H_2 production. *Ceram. Int.* **2023**, *49* (8), 11989−11998.